Article

Differentiation of HSA and BSA and Instantaneous Detection of HSO₃⁻ Using Confined Space of Serum Albumins and Live Cell Imaging of Exogenous/Endogenous HSO₃⁻

Manzoor Ahmad, Nancy Singla, Siloni Singh Bhadwal, Satwinderjeet Kaur, Prabhpreet Singh, and Subodh Kumar*

Read Online

ACCESS | Metrics & More | Article Recommendations | SI Supporting Information

ABSTRACT: The limitations of prevailing probes for the detection of human serum albumin (HSA) and HSO_3^- make it challenging to apprehend the cooperative effect of both HSA and HSO_3^- in biological systems. Herein, we present a multi-responsive fluorescent probe **MGTP**, which distinguishes HSA from bovine serum albumin (BSA) through an ∼104-fold fluorescence enhancement at an emission maximum of 595 nm with HSA and only an ∼10-fold increase at an emission maximum of 615 nm with a shoulder at 680 nm with BSA. The absorbance spectrum of **MGTP** also discriminates HSA and BSA with the respective absorption maxima at 543 nm and at 580 nm. **MGTP** in the confined space of HSA or BSA undergoes instantaneous conjugate addition of HSO_3^- and results in a ratiometric change in fluorescence intensity with diminishing of red fluorescence (600 nm) and emergence of green fluorescence (515 nm). **MGTP** in the absence of SAs does not react with HSO_3^- in phosphate-buffered saline buffer and reacts sluggishly in the dimethyl sulfoxide−water 1:1 mixture. The limit of detection values for the detection of HSA and HSO_3^- are 4 and 6.88 nM, respectively. The drug binding studies reveal that **MGTP** preferably confines itself at the bilirubin site of HSA. In MCF-7 cancer cells, **MGTP** is localized into mitochondria and reveals both exogenous and endogenous visualization of HSO_3^- through a change in fluorescence from the red to green channel.
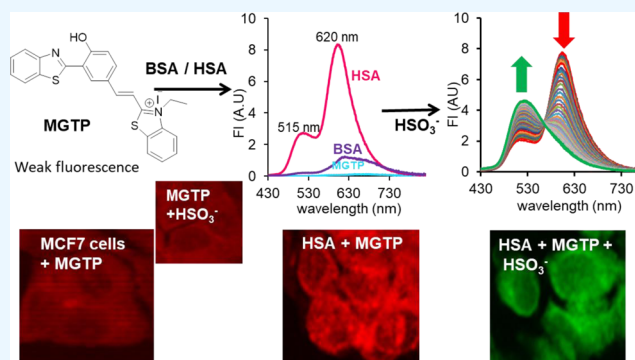
1. INTRODUCTION

The utmost abounding serum protein human serum albumin (HSA) has three homologous helical domains—I, II, and III, each possessing two subdomains—IA, IB, IIA, IIB, IIIA, and IIIB. HSA serves as the depot and carrier protein by reversible interaction of exogenous and endogenous compounds. The transportation of various drugs, metabolites, and fatty acids is carried out by HSA present in blood plasma.[1−5] Any change in the levels of HSA in body fluids is a direct warning for physiological malfunctioning of visceral organs, especially the liver and kidneys.[6] The level of HSA in blood plasma is usually used to screen liver and kidney function and diseases such as coronary heart diseases,[7] multiple myeloma,[8] diabetes mellitus,[9,10] kidney diseases,[11−14] neurometabolic disorders,[15,16] and liver cirrhosis.[17−20] The abnormalities in liver such as cirrhosis or hepatitis can cause hypoproteinemia—a condition with a reduced level of HSA in plasma. Diabetes mellitus, cardiovascular diseases, or renal disorder can cause microalbuminuria—a condition with a high level of HSA in urine. Therefore, detection for urinary albumin is of great clinical importance for diagnosis of albuminuria and related diseases.[21−23]

Sulfur dioxide (SO_2) is a new member of the gasotransmitter[24−26] family in the cardiovascular system and is generated endogenously in cytosols and mitochondria upon the oxidation of sulfur-containing amino acids.[27−29] During respiration, besides CO_2, SO_2 is also breathed out, and the excreta from the kidneys include sulfite and sulfate. In physiological conditions, sulfites are formed by the reaction of SO_2 and water; $SO_2 + H_2O \leftrightarrow H_2SO_3^- \leftrightarrow HSO_3^- + H^+ \leftrightarrow SO_3^{2-} + 2H^+$.[30] The mitochondrial enzyme sulfite oxidase catalyzes the oxidative degradation of cysteine and methionine and also plays a vital role in detoxifying exogenously supplied sulfite from food, pharmaceutical products, and antimicrobial agents.[30,31] However, the deficiency in the sulfite oxidase enzyme or the error in the biosynthetic pathway results in the accumulation of sulfite in biological fluids or tissues.[32−34] The

accumulation of sulfite affects the mitochondrial homeostasis in rat brain mitochondria and also induces mitochondrial swelling and reduces the mitochondrial membrane potential and Ca^{2+} retention capacity.[35] Bisulfite is associated with respiratory abnormalities[36] and brain cancer.[37] Therefore, it is important to develop an effective approach for the determination of bisulfite in biological systems especially, in blood serum.[38−41] Fluorescence is an effective method[42,43] for the detection of analytes, and over the past few years, a number of fluorescent probes have been reported to detect SO_3^{2-}/ HSO_3^-.[44−49] Despite the considerable research studies dedicated toward the pathological and physiological effect of HSO_3^- and HSA, detailed investigation is still required. Despite the collective or cooperative effects and functions of HSA and HSO_3 in biological systems, real-time sensing of both the species still remains an undiscovered area, and strenuous research is needed.

There is only one example in the literature where the cooperative function of HSO_3^- and HSA has been investigated in real-time biological systems. Qu et al. reported a TICT-based probe for the detection of HSA and HSO_3^- simultaneously with a ratiometric change in fluorescence.[50]

Herein, we report a TICT-based multi responsive fluorescent probe **MGTP**, which distinguishes HSA from bovine serum albumin (BSA) by using both UV−vis spectroscopy and fluorescence spectroscopy. **MGTP** with HSA exhibits a 104-fold enhancement in fluorescence with a maximum at 595 nm, while with BSA, it gives only a 10-fold fluorescence enhancement at 615 nm with a shoulder at 680 nm (Scheme 1). **MGTP** in a confined space of HSA/BSA

Scheme 1. Salient Features of Probe MGTP

undergoes instantaneous addition of HSO_3^- resulting in the ratiometric change in fluorescence from orange/red to green in <2 min. **MGTP** is preferably confined at the bilirubin site of HSA or BSA. **MGTP** on incubation with MCF-7 cells reveals

intense red fluorescence in mitochondria, which is further able to detect both exogenous and endogenous HSO_3^- in MCF-7 cells, consistent with the shift in emission from red to green.

2. RESULTS AND DISCUSSION

2.1. Synthesis and Characterization of MGTP. The condensation of **MGZ** with 3-ethyl-2-methylbenzo[d]thiazol-3-ium iodide (**1**) in DMF gave **MGTP**, an orange red solid, in 65% yield (Scheme 2). The ^{1}H NMR spectrum of **MGTP** along with other required signals shows the presence of a 1H doublet at δ 7.94 with the coupling constant $J = 16$ Hz and confirms the trans geometry around the double bond. ^{13}C NMR and high-resolution mass spectrometry (HRMS) data further endorse the structure of **MGTP** (Figures S1−S7).

2.2. Effect of Dimethyl Sulfoxide−Water Binary Mixtures on UV−Vis and Fluorescence Spectra of MGTP. To rationalize the role of water on the photophysical and aggregation properties of **MGTP**, its solutions were prepared in dimethyl sulfoxide (DMSO)−H_2O [phosphate-buffered saline (PBS) buffer, pH 7.4] binary mixtures, and their UV−vis and fluorescence studies were performed. The solutions were allowed to equilibrate at 25 °C for 2 h before recording the data. The UV−vis spectrum of **MGTP** (10 μM) in DMSO displays a high energy band at 385 nm and a low energy band at 585 nm. With a regular increase in f_w, the absorption maximum at 585 nm is gradually blue-shifted with the decrease in absorbance. In DMSO−H_2O (1:9), the low energy absorption maximum is blue-shifted by 75 nm from 585 to 510 nm (Figure 1A). The UV−vis spectrum of **MGTP** (10 μM) in water (99.9%) becomes broad with a shoulder at ∼610 nm. The plot of wavelength of the absorption maximum against f_w shows a gradual blue shift in the absorption band with increasing f_w and is also associated with the decrease in absorbance (Figure 1B). This gradual decrease in absorption and the blue shift in the absorption band of **MGTP** with increasing amounts of water are assigned to the face to face stacking, that is, H-type aggregation, of **MGTP** molecules.[51,52] On excitation at 415 nm, the fluorescence spectrum of **MGTP** (10 μM) in DMSO displays a structured emission band with maxima at 680, 605, and 515 nm. In the DMSO−H_2O (9:1) binary mixture, fluorescence intensity decreases sharply by factors of 12, 6.8, and 55.9, respectively, at 680, 605, and 515 nm (Figure S8) in comparison to that in DMSO. The spectrum showed emission maxima at 617 and 494 nm. The increase in f_w up to 40% results in an increase in fluorescence intensity at 617 nm, and a further increase in f_w causes a gradual decrease in fluorescence intensity (Figure 1C). In 99.9% water, the fluorescence spectrum becomes broad and emits in the region 660−825 nm. The emission maximum wavelength decreases linearly with increasing f_w in DMSO−
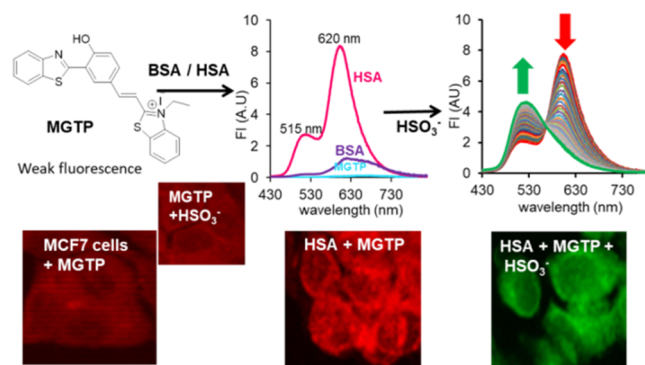
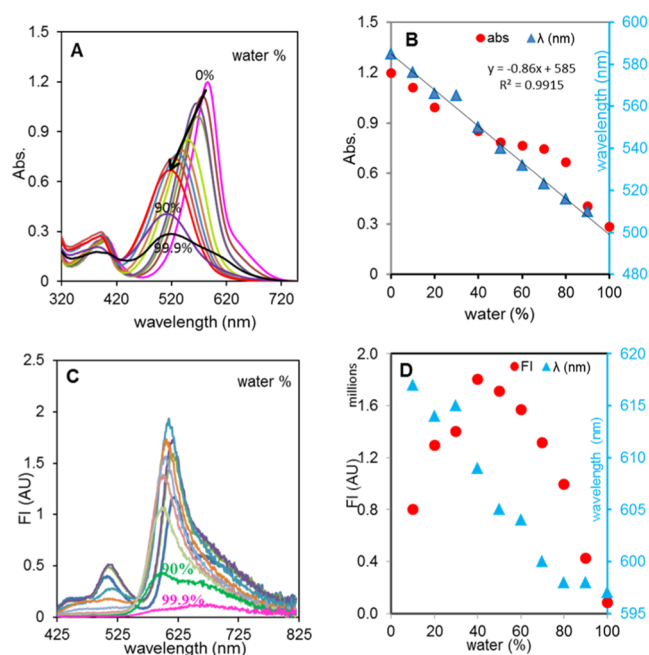**Scheme 2. Synthesis and Michael Addition of HSO_3^- on MGTP**
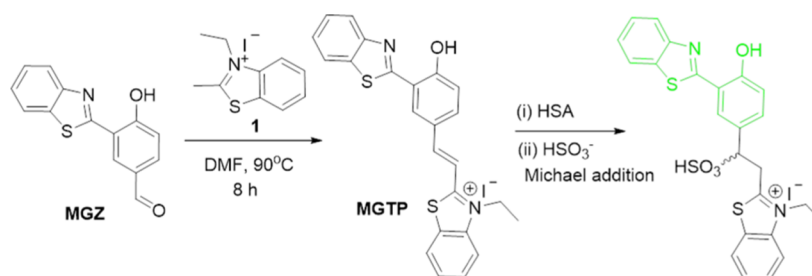
Figure 1. (A) UV−vis spectra of **MGTP** (10 μM) and (B) plot of the maximum absorption wavelength and their respective absorbance vs f_w in DMSO−water binary mixtures; (C) fluorescence spectra of **MGTP** (10 μM), (λ_{ex} = 415 nm); and (D) plot of the emission maximum wavelength and their fluorescence intensity vs f_w in DMSO−water binary mixtures.

H$_2$O binary mixtures (Figure 1D) and is consistent with face to face stacking of **MGTP** molecules, that is, H-type aggregation.

2.3. Differential Spectroscopic Response of MGTP to HSA over BSA and Other Biomolecules. The selectivity of **MGTP** (10 μM, PBS 10 mM, pH 7.4, 0.1% DMSO) toward

serum albumins (SAs) was investigated by UV−vis spectroscopy and fluorescence spectroscopy in the presence of commonly intervening bio-analytes such as trypsin, aspartic acid, histidine, pepsin, lysozyme, bromelain, lysine, and hemoglobin (50 μM each) and was found to show change only with SAs, HSA and BSA (Figure 2A). The UV−vis spectrum of **MGTP** exhibits an absorption band with a maximum at 522 nm along with a shoulder at ∼610 nm. In the presence of has, the absorbance of the 522 nm band increases, associated with the red shift to 543 nm, whereas the shoulder at ∼610 nm disappears. However, BSA exhibits a sharp increase in absorbance at 580 nm, and the absorbance at 522 nm decreases (Figure 2B). The solutions of **MGTP** having HSA and BSA appear red fluorescent under illumination of 365 nm light, whereas the solutions possessing other bio-species appeared non-fluorescent, just like **MGTP** solution. On excitation at 415 nm, **MGTP** with HSA (50 μM) exhibits a 104-fold increase in fluorescence intensity with a maximum at 595 nm, whereas with BSA (50 μM), it results in only a 10-fold increase in fluorescence intensity at 615 nm with a shoulder at 680 nm (Figure 2C). Therefore, both UV−vis and fluorescence spectra can be used to distinctly distinguish between HSA and BSA. HSA and BSA have only ∼76% similar structural and amino acid homology.[53] The 24% variance in the amino acid sequence is responsible for difference in their optical behavior toward **MGTP**. However, there are few probes in the literature that exhibit a higher increase in fluorescence intensity with HSA than with BSA,[22,23] but the discrimination between HSA and BSA with different absorption and emission maxima is not available.

2.4. Quantitative Detection of HSA and BSA with MGTP. **MGTP** (10 μM, PBS 10 mM, pH 7.4, 0.1% DMSO) on excitation at 415/520 nm displays very weak emission with a maximum at 665 nm. On addition of HSA to **MGTP** (λ_{ex} 415
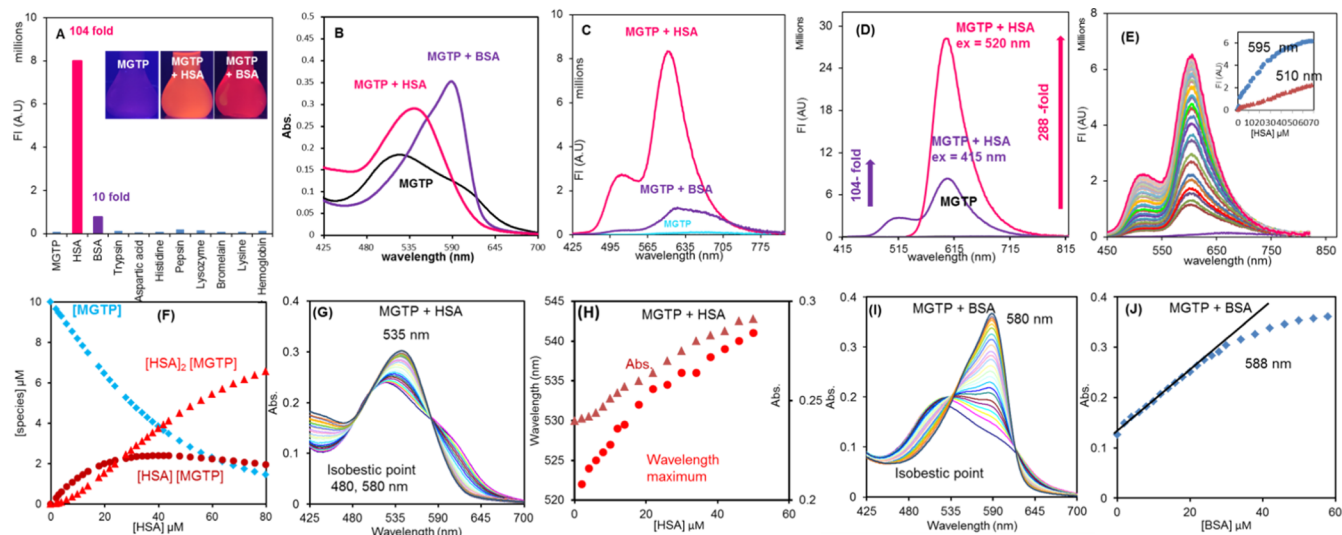

Figure 2. (A) Fluorescence intensity of **MGTP** (10 μM, PBS, pH 7.4, 0.1% DMSO) at 595 nm in the presence of different bio-analytes (50 μM each). Inset: photograph of (left) **MGTP** (10 μM), (middle) **MGTP** (10 μM) + (HSA, 50 μM), and (right) **MGTP** (10 μM) + (BSA, 50 μM), all three in 99.9% PBS. (B) UV−vis spectra of **MGTP** (10 μM) in the absence and the presence of HSA (50 μM) and BSA (50 μM). (C) Fluorescence spectra of **MGTP** (10 μM) with HSA and BSA (50 μM), λ_{ex} 415 nm. (D) Fluorescence spectra of **MGTP** (10 μM, PBS 10 mM, pH 7.4, 0.1% DMSO) with HSA (50 μM) with λ_{ex} values of 415 and 520 nm; (E) change in the fluorescence spectrum of **MGTP** (10 μM, PBS 10 mM, pH 7.4, 0.1% DMSO) with the gradual addition of HSA, λ_{ex} 415 nm, inset: plot of fluorescence intensity vs [HSA] at 595 and 510 nm; and (F) distribution of various stoichiometric species with addition of HSA to **MGTP**. (G,I) Change in the UV−vis spectrum of **MGTP** on gradual addition of (G) HSA and (I) BSA. (H) Plot of the change in wavelength of the absorbance maximum and absorbance at the maximum on addition of aliquots of HSA. (J) Plot of change in absorbance at 588 nm on addition of aliquots of BSA.
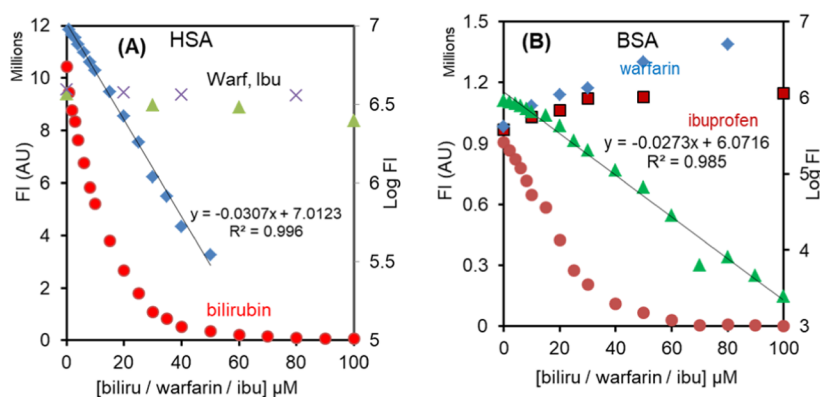
Figure 3. (A) Change in fluorescence of **MGTP** (10 μM)−HSA (50 μM) and (B) change in fluorescence of **MGTP** (10 μM)−BSA (50 μM) in PBS (10 mM, pH 7.4) with bilirubin, warfarin, and ibuprofen. λ_{ex} = 415 nm.

nm), two emission bands at 515 and 695 nm are observed. On using the 520 nm excitation wavelength, only the emission maximum at 595 nm with an enhanced intensity is found (Figure 2D). In order to evaluate the ease in complex formation, HSA (50 μM) was added to **MGTP** (10 μM), and fluorescence spectra were recorded at different intervals of time (λ_{ex} = 415 and 520 nm). It has been found that the fluorescence intensity of the solution increases gradually (Figure S9A) with time and within 20 min of addition of HSA becomes stable. Similarly, BSA (50 μM) with **MGTP** (10 μM) shows an increase in fluorescence with time but requires ~90 min for completion of interaction (Figure S9B). Therefore, the interaction of **MGTP** with HSA is reasonably fast. Upon incremental addition of HSA to **MGTP** (10 μM, PBS 10 mm, pH 7.4, 0.1% DMSO), the fluorescence intensity increases gradually between 0 and 70 μM concentrations of HSA and then achieves a plateau (Figure 2E). The limit of detection (LOD) values as determined (Figure S10) by the equation 3σ/slope are ~4 and ~1 nM, respectively, on using excitation wavelengths of 415 and 520 nm. The LOD for HSA (4 nM), though not best in the literature (0288 nM),[50] is far better than that of HSA present in urine (500 nM). The analysis of these titration data through non-linear regression analysis shows the formation of HSA ∩ **MGTP** (1:1) and (HSA)$_2$ ∩ **MGTP** (2:1) stoichiometric complexes with log $\beta_{[HSA][MGTP]}$ = 4.31 and log $\beta_{[HSA]_2∩[MGTP]}$ = 9.03. The distribution of species depends on the concentration of HSA, that is, at <20 μM HSA, 1:1 species dominates, but at a higher concentration of HSA, the 2:1 species (HSA)$_2$ ∩ **MGTP** is in higher amounts (Figure 2F). Similarly, the incremental addition of BSA to **MGTP** results in a gradual increase in fluorescence between 0 and 70 μM BSA, which then achieves a plateau (Figure S11A,B). The analysis of titration data through non-linear regression analysis shows the formation of BSA ∩ **MGTP** (1:1) and (BSA)$_2$ ∩ **MGTP** (2:1) stoichiometric complexes with log $\beta_{[BSA][MGTP]}$ = 4.47 and log $\beta_{[BSA]2∩[MGTP]}$ = 8.50 (Figure S11C). The LODs as determined by the equation 3σ/slope are ~45. and ~5 nM, respectively, on using excitation at 415 and 520 nm (Figure S12).

To understand the ground-state interaction of **MGTP** with SAs, we also analyzed the change in the UV−vis spectrum of **MGTP** with HSA and BSA. On addition of HSA (Figure 2G,H), the absorption maximum of **MGTP** at 522 nm is gradually red-shifted with the increase in absorbance, and with 5 equiv of HSA, the absorption maximum shifts from 522 to 543 nm. Two isosbestic points at 480 and 580 nm point to the

equilibrium between reactants and products. Interestingly, on addition of aliquots of BSA to **MGTP**, the absorbance gradually increases at 580 nm up to the addition of 5 equiv of BSA and achieves a plateau (Figure 2I,J). The presence of two isosbestic points at 535 and 619 nm points to the equilibrium between reactants (**MGTP** and BSA) and products. Quite significantly, **MGTP** gives different UV−vis and fluorescence spectra with HSA and BSA and points to the differential interaction of **MGTP** with HSA and BSA.

2.5. Sensing Mechanism of HSA/BSA by MGTP. In general, HSA and BSA possess two highly active binding sites site-I and site-II for selective binding with warfarin and ibuprofen. In recent years, subdomain IB, a bilirubin binding site, has been rationalized for selectivity toward hemin and fusidic acid. To rationalize the binding of **MGTP** with HSA/BSA at these binding sites, the solutions of **MGTP** (10 μM) with HSA (50 μM) and BSA (50 μM) were titrated with site-specific drugs such as bilirubin (subdomain IB), warfarin (sudlow site I, subdomain IIA), and ibuprofen (sudlow site II, subdomain IIIA). The solution of **MGTP** (10 μM)−HSA (50 μM) reveals >99% quenching of fluorescence intensity with bilirubin (50 μM) (Figure 3A). However, warfarin and ibuprofen cause only <10% quenching even when present in 100 μM amounts. The plot of [bilirubin] against log[FI] shows a linear change between 0 and 50 μM bilirubin with R^2 = 0.996. Similarly, fluorescence of the **MGTP** (10 μM)−BSA (50 μM) solution undergoes nearly complete quenching with bilirubin, but warfarin and ibuprofen cause a small fluorescence enhancement. The presence of warfarin and ibuprofen in the **MGTP**−BSA mixture enhances the binding of **MGTP** in BSA at the bilirubin site. The plot of [bilirubin] versus log[FI] reveals a linear change (R^2 = 0.985) between 0 and 100 μM bilirubin (Figure 3B). Therefore, **MGTP** preferably binds at subdomain IB, a bilirubin binding site, in both HSA and BSAs.

The pH of the medium is a microenvironment that considerably affects the photo-physical behavior of a molecule. In order to rationalize the effect of pH, the solutions of **MGTP** in water (1% DMSO) were adjusted to different pH values, and their UV−vis and fluorescence spectra were recorded. UV−vis spectra of **MGTP** (10 μM) on recording at varied pH values between 2 and 11 show the presence of two absorption bands at ~500 and 400 nm. At a pH of 11, the absorption at 500 nm (ϵ = 27,500) is the maximum, and on lowering the pH, it gradually decreases and attains a minimum at a pH of 3 (ϵ = 2000). The absorbance of **MGTP** at 415 nm remains stable between pH values of 6 and 11 (ϵ = 14,000 ± 1000); however,
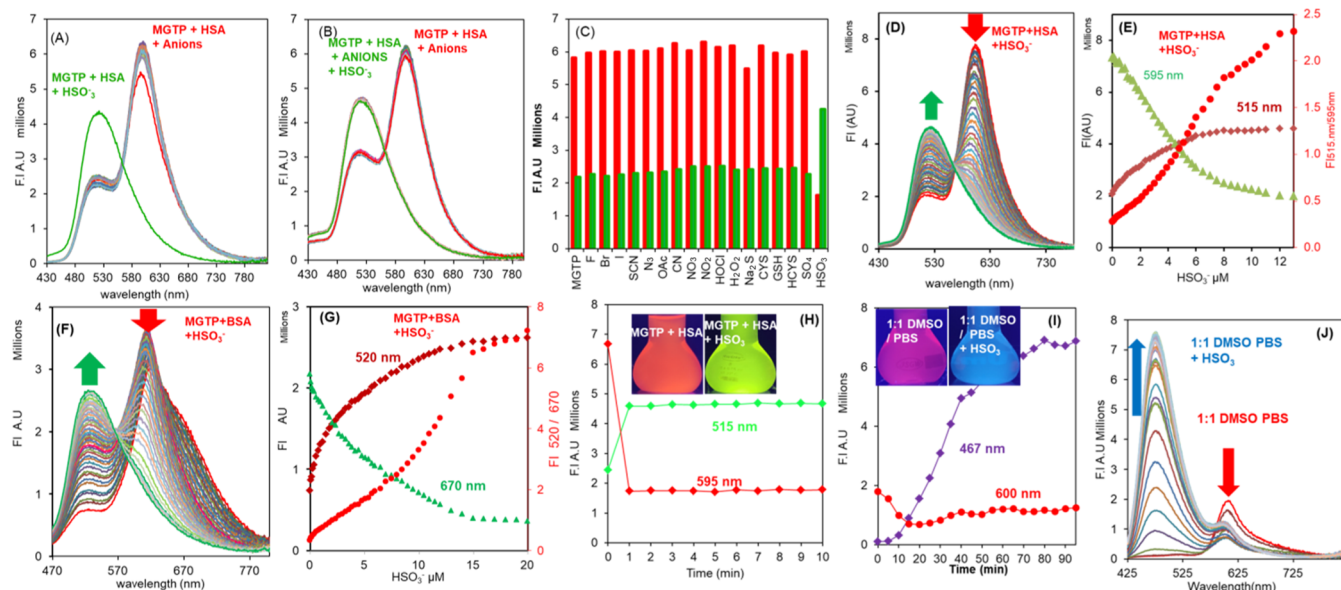
Figure 4. Fluorescence response of **MGTP** (10 μM) + HSA (50 μM) in PBS (10 mM, pH 7.4) (A) toward various anions (100 μM) and (B,C) toward HSO$_3^-$ in the presence of various anions, λ_{ex} 415 nm. (D,F) Spectral response of **MGTP** + HSA (10 μM:50 μM) and **MGTP** + BSA (10 μM:50 μM) on gradual addition of HSO$_3^-$. (E,G) Ratiometric change in fluorescence at 595 and 515 nm on incremental addition of HSO$_3^-$; λ_{ex} 415 nm. (H) Time-dependent change in the fluorescence spectrum of **MGTP** (10 μM) on addition of HSO$_3^-$ (50 μM) in DMSO−PBS (1:1) (10 mM, pH 7.4); inset: (left) photograph of **MGTP** (10 μM) + HSA (50 μM) in 99.9% PBS and (right) **MGTP** (10 μM) + HSA (50 μM) + HSO$_3^-$ (50 μM) in 99.9% PBS. (I) Plot of emission intensity at 467 and 600 nm vs time (min); inset: (left) **MGTP** in 1:1 PBS−DMSO, pH 7.4, and (right) **MGTP** (10 μM) + HSO$_3^-$ (50 μM) in 1:1 PBS−DMSO, pH 7.4. (J) Time-dependent fluorescence spectra of **MGTP** (10 μM) + HSA (50 μM) on addition of HSO$_3^-$, showing the change in emission intensity at 515 and 595 nm vs time (min); λ_{ex} = 415 nm.

on lowering the pH, molar absorptivity gradually increases and reaches 31,500 ± 1000 at a pH of 3 (Figure S13A). **MGTP** (λ_{ex} = 415 nm) gives very weak fluorescence between pH values of 7 and 11, but under acidic conditions, the fluorescence gradually increases with the emission maximum at ~660 nm with a 30-fold increase in fluorescence intensity at a pH of 3 in comparison to that at a pH of 7.0 (Figure S13B,C). The analysis of these fluorescence data through global regression analysis reveals the equilibrium between neutral, mono-cationic, and di-cationic species (Figure S14) with variation in pH values. The fluorescence intensities of **MGTP** ∩ HSA and **MGTP** ∩ BSA also remain stable between pH values of 7 and 11. Therefore, **MGTP** can be used to study interactions with SAs under physiological conditions.

2.6. Response of MGTP toward HSO$_3^-$ and Other Anions. The solution of **MGTP** (10 μM) + HSA (50 μM) in PBS buffer (10 mM, pH 7.4) gives a low energy absorption band at 543 nm, and the color of the solution appears pink. On addition of different analytes (100 μM) F$^-$, Br$^-$, I$^-$, SCN$^-$, N$_3^-$, $^-$OAc, CN$^-$, NO$_3^-$, HOCl, H$_2$O$_2$, Na$_2$S, CYS, HCYS, GSH, and SO$_4^{2-}$, the absorption spectrum or the color of the solution shows practically no change. However, on addition of HSO$_3^-$, the absorbance between 450 and 650 nm is depleted (Figure S15A) and the solution becomes pale yellow. Michael addition (point 2.7, Figures S18 and S19) of HSO$_3^-$ on the double bond breaks the conjugation between hydroxyphenyl benzothiazole and benzothiazolium moieties to deplete the color. In fluorescence experiments, addition of analytes, namely, F$^-$, Br$^-$, I$^-$, SCN$^-$, N$_3^-$, $^-$OAc, CN$^-$, NO$_3^-$, HOCl, H$_2$O$_2$, Na$_2$S, CYS, HCYS, GSH, and SO$_4^{2-}$, (100 μM each), displays no change in fluorescence emission at 595 and 515 nm. However, on addition of HSO$_3^-$, the fluorescence intensity at 595 nm is completely diminished and that at 515 nm is enhanced (Figure 4A). This results in a change in

fluorescence color of solution from red to green. To check the interference of different analytes in the detection of HSO$_3^-$, the solutions of **MGTP** (10 μM) + HSA (50 μM) in PBS buffer (10 mM, pH 7.4) possessing (100 μM each) F$^-$, Br$^-$, I$^-$, SCN$^-$, N$_3^-$, $^-$OAc, CN$^-$, NO$_3^-$, HOCl, H$_2$O$_2$, Na$_2$S, CYS, HCYS, GSH, and SO$_4^{2-}$ (100 μM) were treated with HSO$_3^-$ (50 μM). It is found that none of the anions interfere in the fluorescence-based detection of HSO$_3^-$ (Figure 4B). The plot of intensities of these spectra at 595 nm (red bars) and 515 nm (green bars) clearly shows the selectivity of probe **MGTP** toward HSO$_3^-$ (Figure 4C). On gradual addition of aliquots of HSO$_3^-$, to the solution of **MGTP** (10 μM) + HSA (50 μM), the simultaneous decrease and increase in the emission intensity, respectively, at 595 and 515 nm are observed (Figure 4D). The plot of ratio of fluorescence intensity (FI$_{515nm/595nm}$) against [HSO$_3^-$] displays a linear relationship (R^2 = 0.9901) between 0 and 4 μM concentrations of HSO$_3^-$ (Figure 4E). The LOD for HSO$_3^-$ is determined to be 6.68 nM according to the equation 3σ/slope (Figure S15B), which is much better than reported earlier[43−50] in the presence of HSO$_3^-$. The very low detection limit provides an edge for **MGTP** to determine HSO$_3^-$ in living systems under physiological conditions. Similarly, the solution of **MGTP** + BSA (1:5) in PBS buffer (99.9%) on titration with HSO$_3^-$ in a cuvette exhibits the simultaneous decrease and increase in fluorescence intensity, respectively, between 600−700 and 500−580 nm regions (Figure 4F,G). /the LOD is determined to be 10 nM according to the equation 3σ/slope. The bright pink (day light) and red (365 nm light) fluorescent solution of **MGTP** (10 μM, PBS (10 mM, pH 7.4) and HSA (50 μM) on addition of HSO$_3^-$ (50 μM) becomes green fluorescent within 30 s (Figures 4H and S16A). Therefore, encapsulation of **MGTP** in HSA facilitates the addition of HSO$_3^-$ on it.[54,55] On keeping the solution for 30 min further, no change in

fluorescence intensity at 595 nm or at 515 nm is observed. The solution **MGTP** (10 μM, PBS buffer 10 mM, pH 7.4) appears purple in day light and on addition of different species including HSO_3^- does not show any change in its color, even on keeping for 24 h (Figure S16B). In buffer, **MGTP** exists as aggregates with a hydrodynamic diameter of 802.6 nm (Figure S17), and these aggregates restrict the addition of HSO_3^- on the double bond. We also evaluated the addition of HSO_3^- in the molecularly dissolved state of **MGTP**. **MGTP** (10 μM) in DMSO−PBS (1:1) on addition of HSO_3^- (50 μM) undergoes a change in its fluorescence from red to cyan ($\lambda_{em.}$ = 467 nm) but requires >60 min for the completion of the addition process (Figure 4I,J).

2.7. Reaction Mechanism of MGTP with HSO_3^-. The sensing mechanism of **MGTP** for the detection of bisulfite has been examined by ^{1}H NMR and HRMS studies. On addition of HSO_3^- to **MGTP** (DMSO-d_6−water, 9:1) (Figure S18), the proton signals were in general shifted up-field. In the ^{1}H NMR spectrum of **MGTP**, the proton signal at δ 7.95 (H_c) is assigned to the alkene moiety on the basis of the coupling constant J = 16 Hz. On addition of HSO_3^-, this signal disappears and new signals appear at δ 4.30 ($H_{b'}$, 2H) and δ 4.08 ($H_{a'}$, 1H). The presence of these 2H and 1H signals clearly indicates that the double bond undergoes Michael type addition by HSO_3^-, and the 1H singlet at δ 9.85 (H_d) corresponds to HSO_3^-. The change in fluorescence color of the solution in the NMR tube from red (only **MGTP**) to cyan (**MGTP** + HSO_3^-) resembles the phenomenon that occurred in the DMSO−buffer (1:1) mixture. The similar blue shift in the fluorescence (Figure 4D) on addition of HSO_3^- to **MGTP**−HSA solution corroborates the Michael type addition of HSO_3^- to **MGTP** in the presence of HSA. The HRMS spectrum of **MGTP** exhibits a parent peak at 415.0915 corresponding to the $[C_{26}H_{21}N_2O_2S^+]$, **MGTP** moiety. After the addition of 2 equiv of HSO_3^-, two new peaks appear at 497.0614 and 519.0469, corresponding to **MGTP**−HSO_3^- and **MGTP**−SO_3Na, respectively (Figure S19). All these experimental results corroborate that **MGTP** undergoes Michael addition with HSO_3^-.

2.8. Fluorescence Imaging of Exogenous and Endogenous HSO_3^- in MCF-7 Cells. Before bio-imaging experiments, in vitro cytotoxicity of **MGTP** in MCF-7 cell lines was evaluated using a standard MTT assay. MCF-7 cells treated with **MGTP** (50 μM) for 24 h show >80% cell viability, which demonstrate the low toxicity of **MGTP**-treated cells. MCF-7 cells on incubation with **MGTP** (10 μM) for 1 h display fluorescence in the red channel and a very weak fluorescence in the green channel (Figure 5A_1−A_4). MCF-7 cells on incubation with HSA (50 μM) for 3 h followed by the incubation with **MGTP** (10 μM) for 1 h (Figure 5, compare C_3 with A_3) exhibit strong fluorescence in the red channel and a weak fluorescence in the green channel. MCF-7 cells pretreated with HSA (50 μM, 3 h) and HSO_3^- (50 μM) for 1 h display almost no fluorescence in the red channel and a strong fluorescence in the green channel (Figure 5D_2,D_3).

These results clearly show the conjugate addition of HSO_3^- on **MGTP** molecules in MCF-7 cells in the presence of HSA. We further studied the endogenous generation of HSO_3^- by incubation of MCF-7 cells with GSH (500 μM) and $Na_2S_2O_3$ (250 μM). The incubation of MCF-7 cells with HSA (50 μM, 3 h) and **MGTP** (10 μM, 1 h) and then with GSH (500 μM)/ $Na_2S_2O_3$ (250 μM) again result in the depletion of red fluorescence and the appearance of green fluorescence.

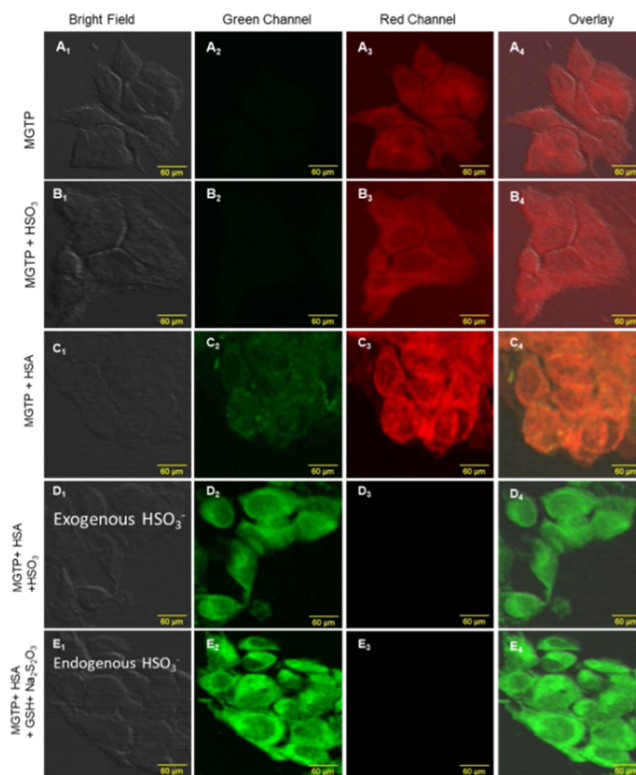**Figure 5.** Images of MCF-7 cells (A_1−A_4) only incubated with **MGTP** (10 μM) for 1 h; (B_1−B_4) incubated with **MGTP** (10 μM) for 1 h and then with HSO_3^- (50 μM) for 3 h; (C_1−C_4) incubated with HSA (50 μM) for 3 h and then with **MGTP** (10 μM) for 1 h; (D_1−D_4) incubated with HSA (50 μM) for 3 h and then with **MGTP** (10 μM) for 1 h and further treated with exogenous HSO_3^- (50 μM) for 3 h; and (E_1−E_4) incubated with HSA (50 μM) for 3 h and then with **MGTP** (10 μM) for 1 h and further treated with GSH (500 μM)/$Na_2S_2O_3$ (250 μM) for 3 h (endogenous generation of HSO_3^-). Scale bar: 60 μM.

Significantly, incubation with GSH (500 μM) and $Na_2S_2O_3$ (250 μM) releases HSO_3^- endogenously, which on conjugate addition on **MGTP** gives green fluorescence (Figure 5E_1−E_4). In order to rationalize the role of HSA on bio-imaging of HSO_3^-, we also studied the incubation of MCF-7 cells with **MGTP** and HSO_3^- (50 μM, 3 h), without incubation with HSA. Quite significantly, no change in fluorescence in the red channel is observed for MCF-7 not incubated with HSA on treatment with HSO_3^- (50 μM) (Figure 5B_1−B_4). These results clearly show that the sequential interaction of **MGTP** with HSA and then with HSO_3^- gives, respectively, red and green emissions.

The benzothiazolium salts are known to be selectively internalized by the mitochondria of the cells. The co-staining of MCF-7 cells with **MGTP** (10 μM) and commercial MitoTracker green (500 nM) for 1 h gives a Pearson coefficient of 0.884 between green (MitoTracker) and red (**MGTP**) and confirms the good mitochondrial specificity of **MGTP** in MCF-7 cells (Figure 6A_1−A_5). MCF-7 cells incubated with HSA and then co-stained with **MGTP** and MitoTracker green give a Pearson coefficient value of 0.94 between the fluorescence in the red and green channels (Figure 6B_1−B_5).The MCF-7 cells incubated with HSA, then with **MGTP** and Mito Red, and then with GSH (500 μM)− $Na_2S_2O_3$ (250 μM) give a Pearson coefficient of 0.893 (Figure 6C_1−C_5). These results clearly define that the selective
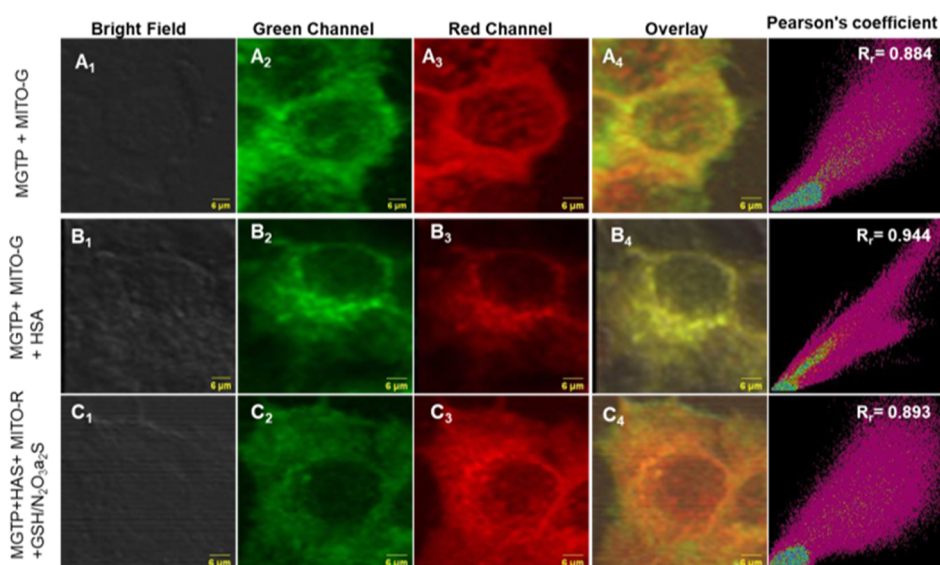
Figure 6. Images of MCF-7 cells incubated with (A_1−A_4) **MGTP** (10 μM) and MitoTracker green (500 nM); (B_1−B_4) HSA (50 μM) for 3 h, then with **MGTP** (10 μM) and MitoTracker green (500 nM) for 1 h, and then with HSO_3^- (50 μM) for 3 h; and (C1 to C4) HSA (50 μM) for 3 h, then with **MGTP** (10 μM), MitoTracker red (500 nM) for 1 h, and then with GSH (500 μM)−$Na_2S_2O_3$ (250 μM). LASER 405, 488 nm. Scale bar: 6 μM.

internalization of **MGTP** in mitochondria is also followed by its interaction with HSA and HSO_3^- in the mitochondria of MCF-7 cells.

3. CONCLUSIONS

Thus, the multi-responsive fluorescent probe **MGTP** discriminates between HSA and BSA through the respective ~100-fold and ~10-fold increases at 595 nm with HSA and broadening of emission with a shoulder at 680 nm with BSA. HSA and BSA could also be differentiated by their respective UV−vis maxima at 543 and at 580 nm. **MGTP** in the confined space of HSA or BSA undergoes instantaneous conjugate addition of HSO_3^- and results in a ratiometric change in fluorescence intensity with diminishing of red fluorescence (600 nm) and emergence of green fluorescence (515 nm). LOD values for the detection of HSA and HSO_3^- are 4 nM and 6.88 nM, respectively. In MCF-7 cancer cells, **MGTP** is localized into mitochondria and finds application for bio-imaging of both exogenous and endogenous HSO_3^- through the change in fluorescence from red to green.

4. EXPERIMENTAL SECTION

4.1. Materials and Equipment. All chemicals were purchased from Spectrochem and Sigma-Aldrich and were used as received. **MGZ** was synthesized by the reported procedure given in Supporting Information Section S2. Thin-layer chromatography was performed on aluminum sheets coated with silica gel 60F254 (Merk, Darmstadt). Deionized water was obtained from an ULTRA UV/UF Rions Lab Water system Ultra 370 series. NMR spectra were recorded on a JEOL 400 MHz NMR spectrometer with TMS as the internal standard. Mass spectra were obtained from a mass Bruker micro TOF QII mass spectrometer. Absorption spectra were recorded on a SHIMADZU-2450 spectrometer equipped with a Peltier system as the temperature controller. Fluorescence spectra were recorded on a Fluorolog Horiba scientific model: FL-1039A/40A. Quartz cuvettes of 1 cm path length were used for the absorbance and fluorescence measurements. Dynamic

light scattering (DLS) measurements were performed at 25.0 + 0.1 °C using a Zetasizer nano ZS instrument. The details of preparation of stock solutions, recording of UV−visible and fluorescence spectra, DLS studies, determination of the detection limit and binding constants, and stoichiometry and drug binding studies of **MGTP**−HSA with warfarin, ibuprofen, and bilirubin are given in the Supporting Information

4.2. Synthesis of MGTP. The solution of MGZ (256 mg, 1 mmol) and 3-ethyl-2-methyl benzothiazolium iodide (305 mg, 1 mmol) in DMF (3 mL) was stirred at 90 °C for 8 h. The brick red solid separated was filtered and was recrystallized from ethanol to get pure compound **MGTP**. Yield 83%, 450 mg, ^{1}H NMR (DMSO-d_6, 400 MHz, ppm): δ 1.49 (t, J = 7.2 Hz, 3H, CH₃), 4.97 (q, J = 7.2 Hz, 2H, CH₂), 7.24 (d, J = 8.8 Hz, 1H, ArH), 7.49 (t, J = 7.2 Hz, 1H, ArH), 7.59 (t, J = 7.2 Hz, 1H, ArH), 7.78 (t, J = 7.2 Hz, 1H, ArH), 7.87 (t, J = 7.2 Hz, 1H, ArH), 7.94 (d, J = 16, 1H, CH=CH), 8.11 (d, J = 8 Hz, 1H, ArH), 8.19 (d, J = 8 Hz, 2H, ArH), 8.26−8.30 (m, 2H, ArH), 8.42 (d, J = 7.6 Hz, 1H, ArH), 8.86 (d, J = 2 Hz, 1H, ArH); ^{13}C NMR (DMSO-d_6, 100 Hz, ppm): 14.29, 44.46, 111.15, 113.97, 116.52, 117.96, 119.39, 122.15, 124.42, 125.30, 126.12, 126.61, 128.19, 129.46, 132.48, 134.76, 140.87, 149.06, 150.61, 151.30, 159.82, 163.41, 167.96, 171.68 HRMS $C_{26}H_{21}N_2O_2S^+$ requires exact mass 415.0933 M$^+$; found (M$^+$) at 415.0920.

■ ASSOCIATED CONTENT

ⓈI Supporting Information

The Supporting Information is available free of charge at https://pubs.acs.org/doi/10.1021/acsomega.2c07163.

> Experimental details; ^{1}H and ^{13}C NMR of starting materials and probe **MGTP**; HRMS spectra of **MGTP** ; fluorescence spectra of **MGTP**; fluorescence intensity of **MGTP** with HSA and BSA with time; fluorescence intensity versus [HSA], λ_{ex} = 415 nm, and fluorescence intensity versus [HSA], λ_{ex} = 520 nm; fluorescence spectra and distribution of various stoichiometric species of **MGTP** with BSA; fluorescence intensity versus [BSA]

plot; absorption and fluorescence spectra of **MGTP** at different pH values; effect of pH on protonation of **MGTP**; UV−vis spectra of **MGTP** (10 μM) + HSA (50 μM) with HSO_3^-; time-dependent fluorescence spectra of **MGTP** (10 μM) + HSA (50 μM) with HSO_3^- (100 μM); DLS studies and the Tyndall effect of **MGTP** (10 μM) in 99.9% water; ^{1}H NMR spectra of **MGTP** and **MGTP** + HSO_3^-; and HRMS spectra of **MGTP** + HSO_3^- (PDF)

■ AUTHOR INFORMATION

Corresponding Author

Subodh Kumar − *Department of Chemistry, Guru Nanak Dev University, Amritsar 143005, India;* ⦿ orcid.org/0000-0003-0874-8163; Email: subodh.chem@gndu.ac.in, subodh_gndu@yahoo.co.in

Authors

Manzoor Ahmad − *Department of Chemistry, Guru Nanak Dev University, Amritsar 143005, India;* ⦿ orcid.org/0000-0002-4878-0996

Nancy Singla − *Department of Chemistry, Guru Nanak Dev University, Amritsar 143005, India*

Siloni Singh Bhadwal − *Department of Botanical and Environment Science, Guru Nanak Dev University, Amritsar 143005, India*

Satwinderjeet Kaur − *Department of Botanical and Environment Science, Guru Nanak Dev University, Amritsar 143005, India*

Prabhpreet Singh − *Department of Chemistry, Guru Nanak Dev University, Amritsar 143005, India;* ⦿ orcid.org/0000-0003-0542-6513

Complete contact information is available at:
https://pubs.acs.org/10.1021/acsomega.2c07163

Notes

The authors declare no competing financial interest.

■ ACKNOWLEDGMENTS

■ REFERENCES

(1) Aguilera-Garrido, A.; del Castillo-Santaella, T.; Yang, T.; Galisteo-González, F.; Gálvez-Ruiz, M. J.; Molina-Bolívar, J. A.; Holgado-Terriza, J. A.; Cabrerizo-Vílchez, M. Á.; Maldonado-Valderrama, J. Applications of serum albumins in delivery systems: Differences in interfacial behaviour and interacting abilities with polysaccharides. *Adv. Colloid Interface Sci.* **2021**, *290*, 102365.

(2) Chen, Q.; Liu, Z. Albumin Carriers for Cancer Theranostics: A Conventional Platform with New Promise. *Adv. Mater.* **2016**, *28*, 10557−10566.

(3) Hu, H.; Quintana, J.; Weissleder, R.; Parangi, S.; Miller, M. Deciphering albumin-directed drug delivery by imaging. *Adv. Drug Delivery Rev.* **2022**, *185*, 114237.

(4) Bal, W.; Sokołowska, M.; Kurowska, E.; Faller, P. Binding of Transition Metal Ions to Albumin: Sites, Affinities and Rates. *Biochim. Biophys. Acta* **2013**, *1830*, 5444−5455.

(5) Ximenes, V. F. Concomitant binding of two fluorescent probes at site-I of human serum albumin: The protein acting as a scaffold enabling fluorescence resonance energy transfer. *J. Photochem. Photobiol., B* **2022**, *234*, 112542.

(6) Gansevoort, R. T.; Correa-Rotter, R. R.; Hemmelgarn, B. R.; Jafar, T. H.; Heerspink, H. J. L.; Mann, J. F.; Matsushita, K.; Wen, C. P. Chronic kidney disease and cardiovascular risk: epidemiology, mechanisms, and prevention. *Lancet* **2013**, *382*, 339−352.

(7) Arques, S. Human Serum Albumin in Cardiovascular Diseases. *Eur. J. Intern. Med.* **2018**, *52*, 8−12.

(8) Kim, J. E.; Yoo, C.; Lee, D. H.; Kim, S.; Lee, J.; Suh, C. Serum Albumin Level Is a Significant Prognostic Factor Reflecting Disease Severity in Symptomatic Multiple Myeloma. *Ann. Hematol.* **2010**, *89*, 391−397.

(9) Neelofar, K.; Ahmad, J. An overview of in vitro and in vivo glycation of albumin: a potential disease marker in diabetes mellitus. *Glycoconjugate J.* **2017**, *34*, 575−584.

(10) Bhat, S.; Jagadeeshaprasad, M. G.; Venkatasubramani, V.; Kulkarni, M. J. Abundance Matters: Role of Albumin in Diabetes, a Proteomics Perspective. *Expert Rev. Proteomics* **2017**, *14*, 677−689.

(11) Shibata, A.; Ishima, Y.; Ikeda, M.; Sato, H.; Imafuku, T.; Chuang, V. T. G.; Ouchi, Y.; Abe, T.; Watanabe, H.; Ishida, T.; Otagiri, M.; Maruyama, T. Human Serum Albumin Hydropersulfide Is a Potent Reactive Oxygen Species Scavenger in Oxidative Stress Conditions Such as Chronic Kidney Disease. *Biochem. Biophys. Res. Commun.* **2016**, *479*, 578−583.

(12) Zhu, T.; Du, J.; Cao, W.; Fan, J.; Peng, X. Microenvironment-Sensitive Fluorescent Dyes for Recognition of Serum Albumin in Urine and Imaging in Living Cells. *Ind. Eng. Chem. Res.* **2016**, *55*, 527−533.

(13) Manolis, A. A.; Manolis, T. A.; Melita, H.; Mikhailidis, D. P.; Manolis, A. S. Low serum albumin: A neglected predictor in patients with cardiovascular disease. *Eur. J. Intern. Med.* **2022**, *102*, 24−39.

(14) Alves, F. C.; Sun, J.; Qureshi, A. R.; Dai, L.; Snaedal, S.; Bárány, P.; Heimbürger, O.; Lindholm, B.; Stenvinkel, P. The Higher Mortality Associated with Low Serum Albumin Is Dependent on Systemic Inflammation in End-Stage Kidney Disease. *PLoS One* **2018**, *13*, No. e0190410.

(15) Li, L.; Liu, B.; Lu, J.; Jiang, L.; Zhang, Y.; Shen, Y.; Wang, C.; Jia, W. Serum albumin is associated with peripheral nerve function in patients with type 2 diabetes. *Endocrine* **2015**, *50*, 397−404.

(16) Hu, Y.; Wang, J.; Zeng, S.; Chen, M.; Zou, G.; Li, Y.; Zhu, L.; Xu, J. Association Between Serum Albumin Levels and Diabetic Peripheral Neuropathy Among Patients with Type 2 Diabetes: Effect Modification of Body Mass Index. *Diabetes, Metab. Syndr. Obes.: Targets Ther.* **2022**, *15*, 527−534.

(17) Arroyo, V.; García-Martinez, R.; Salvatella, X. Human serum albumin, systemic inflammation, and cirrhosis. *J. Hepatol.* **2014**, *61*, 396−407.

(18) Valerio, C.; Theocharidou, E.; Davenport, A.; Agarwal, B. Human albumin solution for patients with cirrhosis and acute on chronic liver failure: Beyond simple volume expansion. *World J. Hepatol.* **2016**, *8*, 345−354.

(19) Naldi, M.; Baldassarre, M.; Domenicali, M.; Bartolini, M.; Caraceni, P. Structural and functional integrity of human serum albumin: Analytical approaches and clinical relevance in patients with liver cirrhosis. *J. Pharm. Biomed. Anal.* **2017**, *144*, 138−153.

(20) Fanali, G.; di Masi, A.; Trezza, V.; Marino, M.; Fasano, M.; Ascenzi, P. Human serum albumin: From bench to bedside. *Mol. Aspect. Med.* **2012**, *33*, 209−290.

(21) Zhao, X.; Zheng, W.; Qin, T.; Du, X.; Lei, Y.; Lv, T.; Zhou, M.; Xu, Z.; Wang, L.; Liu, B.; Peng, X. An anti-interference fluorescent probe for point-of-care diagnosis of albuminuria. *Sens. Actuators, B* **2022**, *351*, 130980.

(22) Fan, J.; Sun, W.; Wang, Z.; Peng, X.; Li, Y.; Cao, J. A fluorescent probe for site I binding and sensitive discrimination of HSA from BSA. *Chem. Commun.* **2014**, *50*, 9573−9576.

(23) Reja, S. I.; Khan, I. A.; Bhalla, V.; Kumar, M. A TICT based NIR-fluorescent probe for Human Serum Albumin: A pre-clinical diagnosis in blood serum. *Chem. Commun.* **2016**, *52*, 1182−1185.

(24) Huang, Y.; Zhang, H.; Lv, B.; Tang, C.; Du, J.; Jin, H. Endogenous sulfur dioxide is a new gasotransmitter with promising

therapeutic potential in cardiovascular system. *Sci. Bull.* **2021**, *66*, 1604−1607.

(25) Du, J.; Huang, Y.; Li, K.; Yu, X.; Jin, H.; Yang, L. Retina-derived endogenous sulfur dioxide might be a novel anti-apoptotic factor. *Biochem. Biophys. Res. Commun.* **2018**, *496*, 955−960.

(26) Biswas, B.; Dogra, S.; Dey, G.; Murugan, N. A.; Mondal, P.; Ghosh, S. Near-infrared emissive cyanine probes for selective visualization of the physiological and pathophysiological modulation of albumin levels. *J. Mater. Chem. B* **2022**, *10*, 3657−3666.

(27) Maiti, B. K. Cross-talk Between (Hydrogen)Sulfite and Metalloproteins: Impact on Human Health. *Chem.—Eur. J.* **2022**, *28*, 202104342.

(28) Kohl, J. B.; Mellis, A.; Schwarz, G. Homeostatic impact of sulfite and hydrogen sulfide on cysteine catabolism. *Br. J. Pharmacol.* **2019**, *176*, 554−570.

(29) Li, Y.; Feng, Y.; Ye, X.; Peng, H.; Du, J.; Yao, X.; Huang, Y.; Jin, H.; Du, J. Endogenous SO2 Controls Cell Apoptosis: The State-of-the-Art. *Front. Cell Dev. Biol.* **2021**, *9*, 729728.

(30) Kappler, U.; Enemark, J. H. Sulfite-oxidizing enzymes. *J. Biol. Inorg Chem.* **2015**, *20*, 253−264.

(31) Eh, M.; Kaczmarek, A. T.; Schwarz, G.; Bender, D. Molecular mechanism of intramolecular electron transfer in dimeric sulfite oxidase. *J. Biol. Chem.* **2022**, *298*, 101668.

(32) Kaczmarek, A. T.; Bender, D.; Gehling, T.; Kohl, J. B.; Daimagüler, H.; Santamaria-Araujo, J. A. S.; Liebau, M. C.; Koy, A.; Cirak, S.; Schwarz, G. A defect in molybdenum cofactor binding causes an attenuated form of sulfite oxidase deficiency. *J. Inherit. Metab. Dis.* **2022**, *45*, 169−182.

(33) Kaczmarek, A. T.; Bahlmann, N.; Thaqi, B.; May, P.; Schwarz, G. Machine learning-based identification and characterization of 15 novel pathogenic SUOX missense mutations. *Mol. Genet. Metab.* **2021**, *134*, 188−194.

(34) Mellis, A.; Roeper, J.; Misko, A. L.; Kohl, J.; Schwarz, G. Sulfite Alters the Mitochondrial Network in Molybdenum Cofactor Deficiency. *Front. Genet.* **2021**, *11*, 594828.

(35) Grings, M.; Moura, A. P.; Amaral, A. U.; Parmeggiani, B.; Gasparotto, J.; Moreira, J. C. F.; Gelain, D. P.; Wyse, A. T. S.; Wajner, M.; Leipnitz, G. Sulfite Disrupts Brain Mitochondrial Energy Homeostasis and Induces Mitochondrial Permeability Transition Pore Opening via Thiol Group Modification. *Biochim. Biophys. Acta, Mol. Basis Dis.* **2014**, *1842*, 1413−1422.

(36) Iwasawa, S.; Kikuchi, Y.; Nishiwaki, Y.; Nakano, M.; Michikawa, T.; Tsuboi, T.; Tanaka, S.; Uemura, T.; Ishigami, A..; Nakashima, H.; Takebayashi, T.; Adachi, M.; Morikawa, A.; Maruyama, K.; Kudo, S.; Uchiyama, I.; Omae, K. Effects of SO 2 on Respiratory System of Adult Miyakejima Resident 2 Years after Returning to the Island. *J. Occup. Health* **2009**, *51*, 38−47.

(37) Sang, N.; Yun, Y.; Li, H.; Hou, L.; Han, M.; Li, G. SO2 Inhalation Contributes to the Development and Progression of Ischemic Stroke in the Brain. *Toxicol. Sci.* **2010**, *114*, 226−236.

(38) Tamima, U.; Singha, S.; Kim, H. R.; Reo, Y. J.; Jun, Y. W.; Das, A.; Ahn, K. H. A benzocoumarin based two-photon fluorescent probe for ratiometric detection of bisulfite. *Sens. Actuators, B* **2018**, *277*, 576−583.

(39) Qin, J.; Kong, F.; Guo, Y.; Wang, D.; Zhang, C.; Li, Y. Rational Construction of a Two-Photon NIR Ratiometric Fluorescent Probe for the Detection of Bisulfite in Live Cells, Tissues, and Foods. *J. Agric. Food Chem.* **2022**, *70*, 7314−7320.

(40) Gao, G.; Wang, J.; Wang, X.; Liu, G.; Fan, L.; Ru, G.; Wang, S.; Song, M.; Shen, W.; Zheng, X.; Han, L.; Liu, L. Reversible Near-Infrared Fluorescent Probe for Rapid Sensing Sulfur Dioxide and Formaldehyde: Recognition and Photoactivation Mechanism and Applications in Bioimaging and Encryption Ink. *Anal. Chem.* **2022**, *94*, 13590−13597.

(41) Tan, L.; Ding, H.; Chanmungkalakul, S.; Peng, L.; Yuan, G.; Yang, Q.; Liu, X.; Zhou, L. A smart TP-FRET-based ratiometric fluorescent sensor for bisulfite/formaldehyde detection and its imaging application. *Sens. Actuators, B* **2021**, *345*, 130331.

(42) Singh, H.; Tiwari, K.; Tiwari, R.; Pramanik, S. K.; Das, A. Correction to Small Molecule as Fluorescent Probes for Monitoring Intracellular Enzymatic Transformations. *Chem. Rev.* **2020**, *120*, 4254−4255.

(43) Ashoka, A. H.; Ali, F.; Tiwari, R.; Kumari, R.; Pramanik, S. K.; Das, A. Recent Advances in Fluorescent Probes for Detection of HOCl and HNO. *ACS Omega* **2020**, *5*, 1730−1742.

(44) Zhang, Y.; Guan, L.; Yu, H.; Yan, Y.; Du, L.; Liu, Y.; Sun, M.; Huang, D.; Wang, S. Reversible Fluorescent Probe for Selective Detection and Cell Imaging of Oxidative Stress Indicator Bisulfite. *Anal. Chem.* **2016**, *88*, 4426−4431.

(45) Zhang, D.; Liu, A.; Ji, R.; Dong, J.; Ge, Y. A Mitochondria-Targeted and FRET-Based Ratiometric Fluorescent Probe for Detection of SO2 Derivatives in Water. *Anal. Chim. Acta* **2019**, *1055*, 133−139.

(46) Agarwalla, H.; Pal, S.; Paul, A.; Jun, Y. W.; Bae, J.; Ahn, K. H.; Srivastava, D. N.; Das, A. A fluorescent probe for bisulfite ions: its application to two-photon tissue imaging. *J. Mater. Chem. B* **2016**, *4*, 7888−7894.

(47) Jiang, C.; Zhang, G.; Peng, G.; Liu, Y.; Kong, Y.; Wang, B. Polymeric Micelles Encapsulating a Small Molecule SO2 Fluorescent Probe Exhibiting Novel Analytical Performance and Enhanced Cellular Imaging Ability. *ACS Appl. Bio Mater.* **2019**, *2*, 236−242.

(48) Yang, S.; Wen, X.; Yang, X.; Li, Y.; Guo, C.; Zhou, Y.; Li, H.; Yang, R. Visualizing Endogenous Sulfur Dioxide Derivatives in Febrile-Seizure-Induced Hippocampal Damage by a Two-Photon Energy Transfer Cassette. *Anal. Chem.* **2018**, *90*, 14514−14520.

(49) Yang, J.; Li, K.; Hou, J.-T.; Li, L.-L.; Lu, C.-Y.; Xie, Y.-M.; Wang, X.; Yu, X.-Q. Novel Tumor-Specific and Mitochondria-Targeted near-Infrared-Emission Fluorescent Probe for SO2 Derivatives in Living Cells. *ACS Sens.* **2016**, *1*, 166−172.

(50) Liang, Z.; Sun, Y.; Zeng, H.; Sun, K.; Yang, R.; Li, Z.; Zhang, K.; Chen, X.; Qu, L. Simultaneous Detection of Human Serum Albumin and Sulfur Dioxide in Living Cells Based on a Catalyzed Michael Addition Reaction. *Anal. Chem.* **2020**, *92*, 16130−16137.

(51) Kwok, E. C.; Tsang, D. P.; Chan, M.; Yam, V. W. Organic Photovoltaic Devices Based on a New Class of Oligothienyleneviny-lene Derivatives as Donor Materials. *Chem.—Eur. J.* **2013**, *19*, 2757−2767.

(52) Spano, F. C. The Spectral Signatures of Frenkel Polarons in H- and J-Aggregates. *Acc. Chem. Res.* **2010**, *43*, 429.

(53) Bujacz, A. Structures of bovine, equine and leporine serum albumin. *Acta Crystallogr. D* **2012**, *68*, 1278−1289.

(54) Zhang, P.; Zhang, Q.; Li, S.; Chen, W.; Guo, X.; Ding, C. Enhanced fluorescence sensing of hypochlorous acid using serum albumin as a signal amplifier. *J. Mater. Chem. B* **2019**, *7*, 1238−1245.

(55) Ma, W.; Du, J.; Yin, J.; Fan, J.; Long, S.; Peng, X. Quantitative recognition and ratiometric cell imaging of HSO_3^- inspired of confined-space based FRET system within human serum albumin. *Sens. Actuators, B* **2018**, *267*, 104−110.